Journal of ELECTRONIC MATERIALS, Vol. 42, No. 2, 2013
DOI: 10.1007/s11664-012-2307-z
© 2012 TMS

Characterization of Recrystallization and Microstructure Evolution in Lead-Free Solder Joints Using EBSD and 3D-XRD

BITE ZHOU,[1,4] THOMAS R. BIELER,[1] TAE-KYU LEE,[2] and WENJUN LIU[3]

1.—Michigan State University, East Lansing, MI 48824, USA. 2.—Cisco Systems, Inc., San Jose, CA 96134, USA. 3.—Advanced Photon Source, Argonne National Laboratory, Argonne, IL 60439, USA. 4.—e-mail: zhoubite@egr.msu.edu

Development of vulnerable high-angle grain boundaries (and cracks) from low-angle boundaries during thermal cycling by means of continuous recrystallization was examined in fine-pitch ball grid array (BGA) packages with Sn-3.0Ag-0.5Cu (wt.%) (SAC305) lead-free solder joints. Electron backscatter diffraction (EBSD) and differential-aperture x-ray microscopy (DAXM or 3D-XRD) were used for surface and subsurface characterization. A large number of subgrain boundaries were observed in the parent orientation using both techniques. However, unlike studies of anisotropic deformation in non-cubic metals at much lower homologous temperatures, no streaked diffraction peaks were observed in DAXM Laue patterns within each 1 μm^3 voxel after thermal cycling, suggesting that geometrically necessary dislocations (GNDs) are effectively absorbed by the preexisting subgrain boundaries. Storage at room temperature ($0.6T_m$) prior to DAXM measurement may also facilitate recovery processes to reduce local GND contents. Heterogeneous residual elastic strains were found near the interface between a precipitated Cu_6Sn_5 particle and the Sn grain, as well as near particular subgrain boundaries in the parent orientation. Grain boundary migration associated with recrystallization resulted in regions without internal strains, subgrain boundaries, or orientation gradients. Development of new grain orientations by continuous recrystallization and subsequent primary recrystallization and grain growth occurred in the regions where the cracks developed. Orientation gradients and subgrain structure were observed within newly formed recrystallized grains that could be correlated with slip systems having high Schmid factors.

Key words: Lead-free solder, Sn crystal orientation, recrystallization, EBSD, synchrotron 3D-XRD, strain

INTRODUCTION

Synchrotron x-ray diffraction (XRD) has been used to characterize melting and solidification behaviors,[1–4] interfacial reactions,[2,5] and intermetallic compounds (IMCs)[6,7] in lead-free solders. In prior studies,[8] microstructure and crystal orientation evolution was examined *in situ* for the full volume of the solder joint using transmission synchrotron XRD. An increase in elastic strain developed after thermal cycling was reported. By focusing the x-ray beam to the submicron scale, microdiffraction techniques can be used to assess the gradients in local strain/stress measurements at the micron scale. One example of using this technique was to study the effects of strain on Sn whisker growth.[9–11]

In this paper, the evolution of recrystallization is examined on a thermally cycled package having a moderately strongly strained package design[12] using

(Received April 29, 2012; accepted September 28, 2012; published online November 10, 2012)

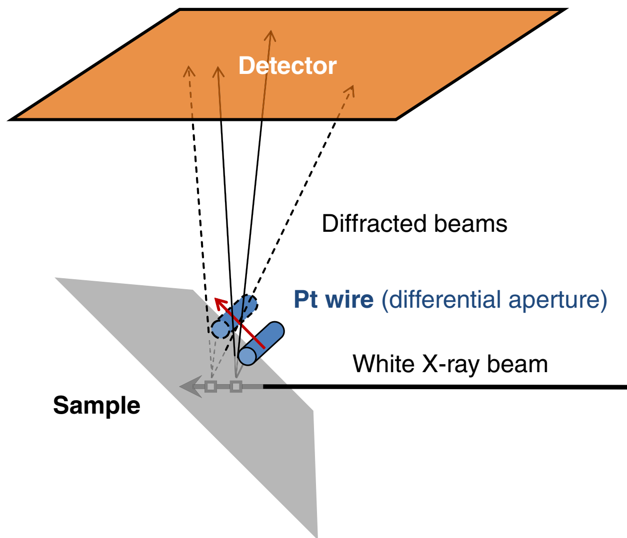

Fig. 1. Schematic showing the experimental setup at Advanced Photon Source beamline 34-ID-E.

conventional EBSD analysis and differential-aperture x-ray microscopy (DAXM, Fig. 1), a form of 3D x-ray diffraction analysis.[13–17] Recrystallization has been identified as a precursor to damage nucleation in lead-free solder joints,[8,18–20] so details of the recrystallization process are sought using the capabilities of 3D x-ray diffraction, which provides the means to measure components of the strain tensor nondestructively,[21] as well as much more accurate angular resolution of local crystal orientations. One particular joint is examined which illustrates several features of recrystallization, such as continuous recrystallization driven by accumulation of dislocations into subgrain boundaries, and also particle-stimulated nucleation where a new orientation developed adjacent to a hard particles,[22,23] and also a combination of primary recrystallization and grain growth.

EXPERIMENTAL PROCEDURES

A schematic of a fine-pitch ball grid array (BGA) package is shown in Fig. 2. The coordinate system used for this analysis is indicated in Fig. 2a. Sn-3.0Ag-0.5Cu (wt.%) (SAC305) lead-free solder joints are used in this package with 0.4 mm ball pitch. Both package and board sides have organic solderability preservative (OSP) surface finish. All of the joints are electrically connected through a daisy-chain. Solder joints were pre-aged at 100°C for 500 h prior to thermal cycling to failure. A 20% increase in resistivity was used as a failure criterion. This package showed the first failure at around 1800 cycles, and the characteristic life cycle number was around 4000 cycles.[12] The package was mounted in epoxy and cross-sectioned, and the outer row of solder joints were polished for scanning electron microscopy (SEM) and electron backscatter diffraction (EBSD) studies. The regions around the solder balls were covered with conductive carbon paint to minimize charging effects. Secondary electron (SE) and backscattered electron (BSE) imaging, and EBSD were obtained using a CamScan 44FE electron microscope. EDAX TSL OIM™ software (version 5.31) was used to generate *c*-axis orientation maps that emphasize the orientation of the crystal *c*-axis with respect to the board interface (prisms are superposed, and color is annotated to assist interpretation of grayscale figures). Raw data were cleaned up using one iteration of "grain dilation" to remove the smallest pixel clusters having a minority orientation. The data were further processed using "neighbor CI correlation" to replace pixels that had low confidence index (CI) with the neighbors that had higher CI.

A bright polychromatic x-ray beam focused to submicron scale (0.5 μm × 0.5 μm) by a pair of Kirkpatrick–Baez (K–B) mirrors was used in beamline 34-ID-E at the Advanced Photon Source (APS) at Argonne National Laboratory. The energy spectra used allows measurements to be made up to about 100 μm beneath the sample surface. A Pt wire was used as a differential aperture, which traverses along the sample surface, blocking a portion of the diffraction beam (Fig. 1). At each step, the position of the wire is recorded and Laue patterns are captured by an area detector. By using a reconstruction algorithm performed on a computer cluster, Laue patterns that come from each ~1 μm^3 diffraction volume element (voxel) were extracted to acquire a depth-resolved diffraction pattern from each voxel.[14–17] The results of automatic indexation were stored in summary files, which were further processed using an analysis package developed by Oak Ridge National Laboratory (ORNL) and APS[24] embedded in Igor Pro (version 6.21; WaveMetrics, Inc.).

The sample was tilted 45° with respect to the incident x-ray beam. Two surface line scans (#1 and #2) were taken across the boundaries between the parent grain (red) and a recrystallized (yellow) grain (Fig. 4). Step sizes of 1 μm and 2 μm were chosen for line scan #1 and #2, respectively. DAXM orientation and strain maps were generated using Igor Pro from the summary files. In the examined area, both the Sn phase and a large Cu_6Sn_5 precipitate are present. Automatic indexation and strain calculation were performed for the Sn phase only. Manual indexation for the Cu_6Sn_5 particle was accomplished with a hexagonal structure ($P6_3/mmc$) for η-Cu_6Sn_5 having lattice parameters of a = 0.4190 nm and c = 0.5086 nm.[25]

RESULTS AND DISCUSSION

As shown in Fig. 2, after aging and thermal cycling, all five joints near the corner of the package cracked. From cross-polarized light micrographs (Fig. 2d), four out of five joints showed apparent recrystallization. *c*-Axis EBSD maps (Fig. 2e) reveal that cracks propagated mainly along recrystallized grain

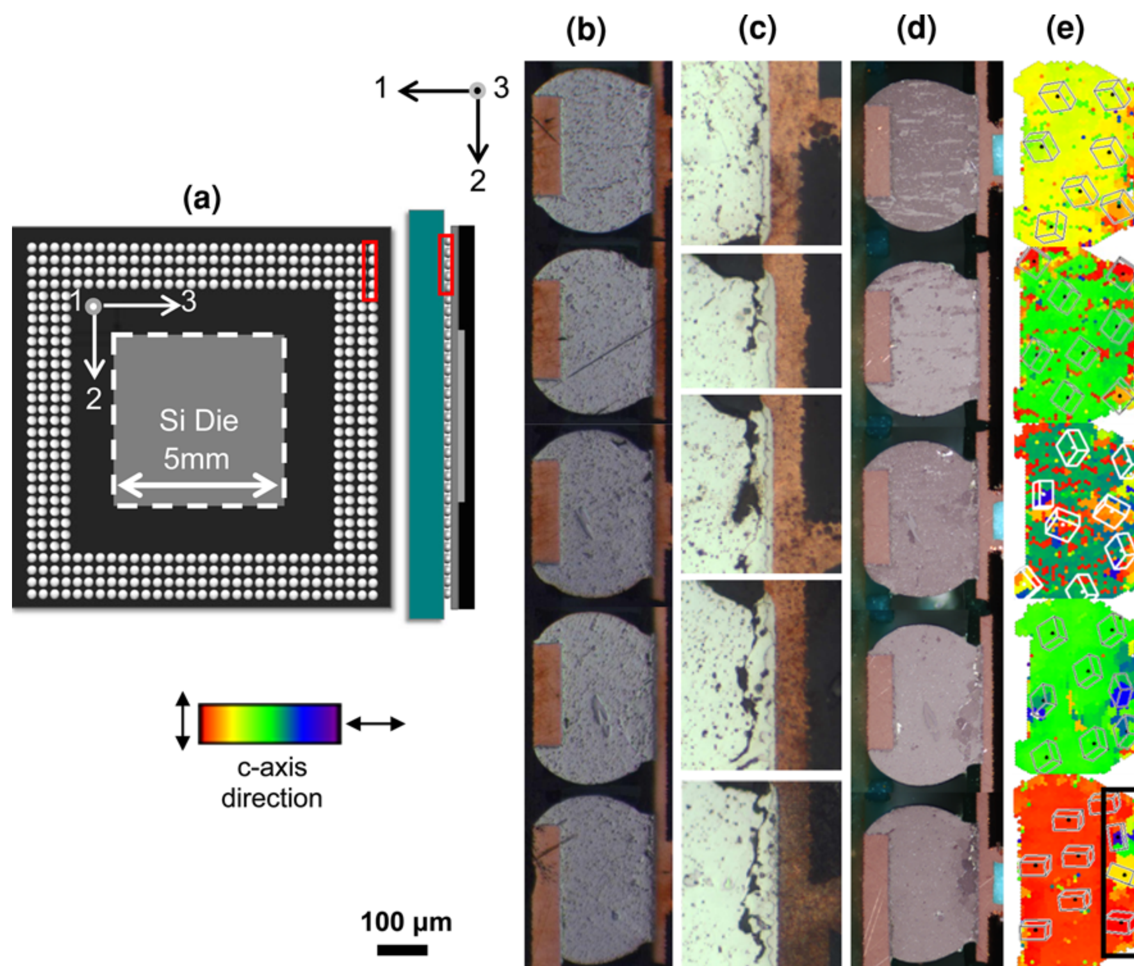

Fig. 2. Fine-pitch (0.4 mm) BGA package with SAC305 solder joints and a small Si die: (a) plan view (looking from the substrate to the chip) and cross-section view of the package; five solder joints at the outermost row are highlighted, and the strain tensor coordinate system is shown inset; (b) optical micrographs; (c) magnified optical images show cracks at the package side; (d) cross-polarized light micrographs; (e) *c*-axis EBSD maps. The interface between ball 5 and the package (black box) is shown in detail in Fig. 3.

boundaries. Recrystallization near the solder/package interface in ball 5 was examined in greater detail using fine-step EBSD and DAXM. In ball 5 (last ball in Fig. 2e), both continuous and discontinuous recrystallization features are evident, as discussed below. This bulk red orientation (with *c*-axis parallel to the interface) has the greatest tensile stress state at the high-temperature part of the cycle.[8]

In Fig. 3, the corresponding optical and BSE images, and EBSD maps for the package side of ball 5 are shown at higher magnification. From the grain boundary map (Fig. 3d), a significant amount of low-angle boundaries (white lines) reside in the lower-right region near the interface, as well as away from the interface, where parent red orientation evolved to an orange orientation by gradual lattice rotation. High-angle boundaries were developed closer to the interface during thermal cycling. As Sn has a number of low-energy (highly favored) special boundary misorientations,[26] gradual misorientation changes will lead to misorientations that have higher boundary energy that may facilitate crack formation and propagation.[27] In the recrystallized area adjacent to cracks, coarsening of IMC particles, as well as an IMC depletion zone, is apparent. This has been reported in literature before.[18,28] A likely outcome of larger spacing between pinning by IMC particles is greater boundary mobility during recrystallization, leading to larger continuously recrystallized grains.[8] Larger grains will result in a larger strain incompatibility arising from elastic and coefficient of thermal expansion (CTE) anisotropy when the misorientation is larger,[29] which can also facilitate crack formation.

A Cu_6Sn_5 particle (as indicated by the lower arrow in Fig. 3c) is located at the boundary between the parent red orientation grain and a recrystallized yellow grain. Fine-step EBSD shows that, adjacent to the Cu_6Sn_5 particle, a small orange orientation is present, which has a twinning relationship with the matrix (red line in Fig. 3d). The nucleation of a significantly different orientation adjacent to a hard particle is indicative of particle-stimulated nucleation, which has been observed in other studies.[23]

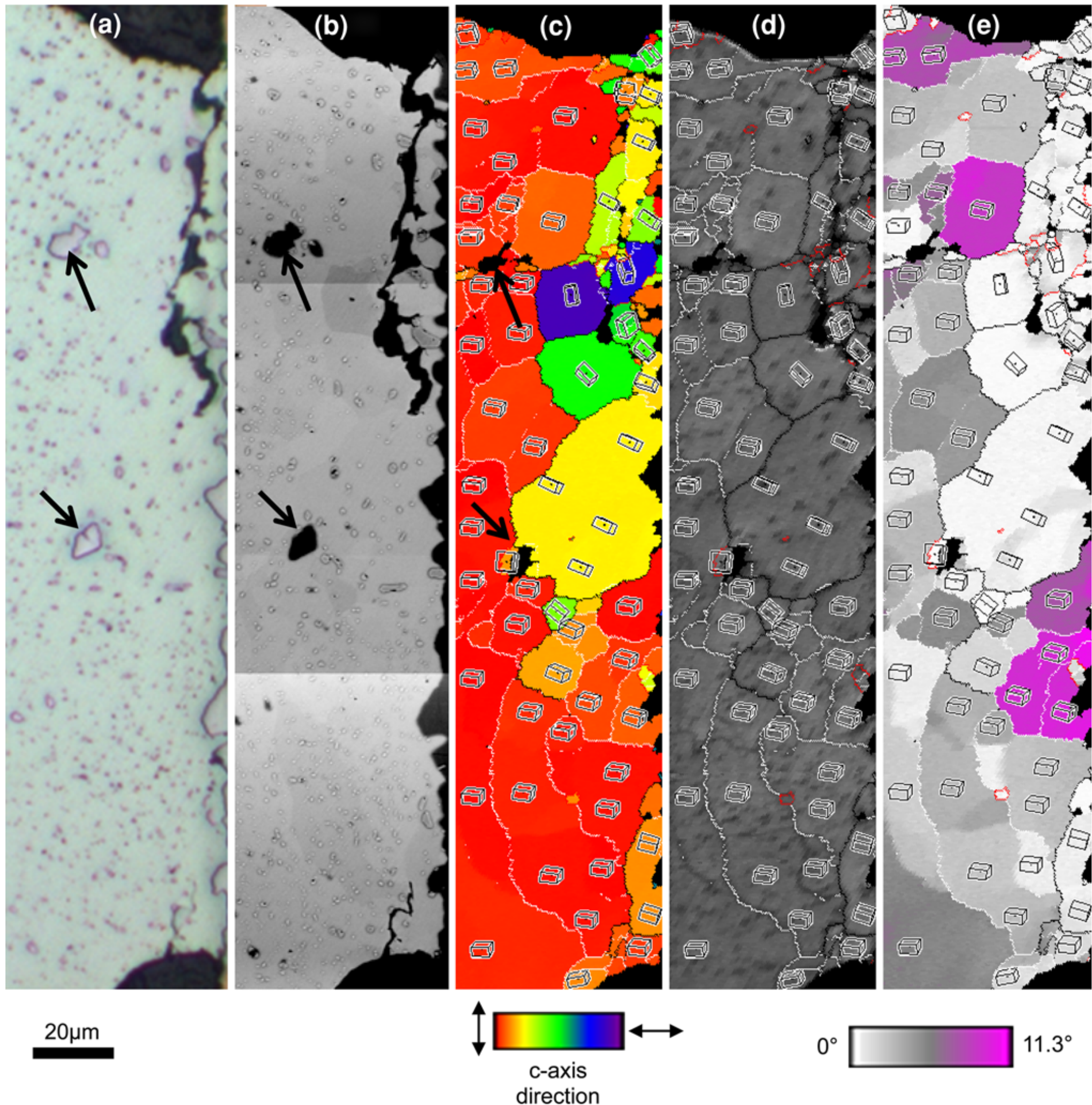

Fig. 3. (a) Optical micrograph, (b) backscatter electron image, and (c) fine-step EBSD *c*-axis map showing recrystallization and cracking; (d) development of high-angle (15° to 55° and 65° to 180°) grain boundaries (black lines) from low-angle (2° to 15°) boundaries (white lines) suggests continuous recrystallization; (e) deviation from grain average orientation, showing subgrain structure; the same Cu_6Sn_5 IMC particles are marked with arrows in different maps.

However, it is not known whether this twin orientation formed by a mechanical twinning process to become a nucleus of a new grain, or if it was initially present adjacent to the particle.

EBSD-BASED ANALYSIS

A grain reference orientation deviation (GROD) map is shown in Fig. 3e. The average orientation in each grain is used as a reference, and the crystal orientation deviation from the average up to 11.3° is represented by a color scale. Figure 3c–e shows that the recrystallized grains surrounding the crack and in the grains just ahead of it exhibit a homogeneous white or light-grey colors in this map, suggesting very low orientation gradients. There are some local regions of lattice rotation adjacent to the crack free surface that reflect crack-tip plasticity at certain points along the fracture path where plastic slip

dissipation may have locally retarded crack growth. In the lower part of the large yellow recrystallized grain in Fig. 3c, e, there is a diffuse band of higher local misorientation, which may be a shear band that precedes formation of a crack.

In contrast, in the parent red orientation, where a large amount of low-angle boundaries are present, much larger orientation deviations and gradients are observed in Fig. 3e. The extent of the deviation varies in different subgrains, and they are separated by sharp subgrain boundaries. The different lattice rotations observed among the subgrains probably arise from the complexity of local stress states during thermal cycling. The amount of lattice rotation varies not only across subgrain boundaries, but also within some of the subgrains.

A fine-step EBSD scan of a smaller area reveals more detailed information about the crystal orientation relationships between different grains as shown in Fig. 4a, where the misorientation angle and rotation axes of selected boundaries are labeled. These misorientations do not correspond with known low-energy boundaries, suggesting that these boundaries are in the midst of increasing misorientation evolution by a continuous recrystallization mechanism (there may be a more energetically favored path to develop recrystallized grains by a two-step lattice rotation about low-index axes, as discussed below).

In Fig. 5a, a GROD map is drawn up to 6.1° spread from the average grain orientation. The local average misorientation (LAM) histogram shows the distribution of the average misorientation angles between each data point up to its third nearest-neighbor pixels. The LAM histogram (Fig. 5b) reflects the spread of Sn crystal orientations due to the presence of geometrically necessary dislocations (GNDs). Despite the difference in the GROD maps, relatively sharp peaks are observed for both parent and recrystallized grains (Fig. 5), suggesting low GND contents. This is further supported by DAXM Laue patterns, as discussed below. Nevertheless, the broader LAM peak and a slight decrease in peak height in parent orientation argue for a difference in dislocation arrangement in the parent and recrystallized grains.

Comparing the two grains in Fig. 5a, it is apparent that a much larger orientation gradient is present in the parent orientation, as there is more variation in color (as also reflected in the extended tail to the right in the histogram in Fig. 5b). However, the boundaries between the differently colored regions are sharp and thereby define distinct subgrain boundary structures in the parent grain. These effects are also evident in Fig. 5c, where the (001), (100), and (010) poles for the parent and recrystallized grain are overlaid. In the parent

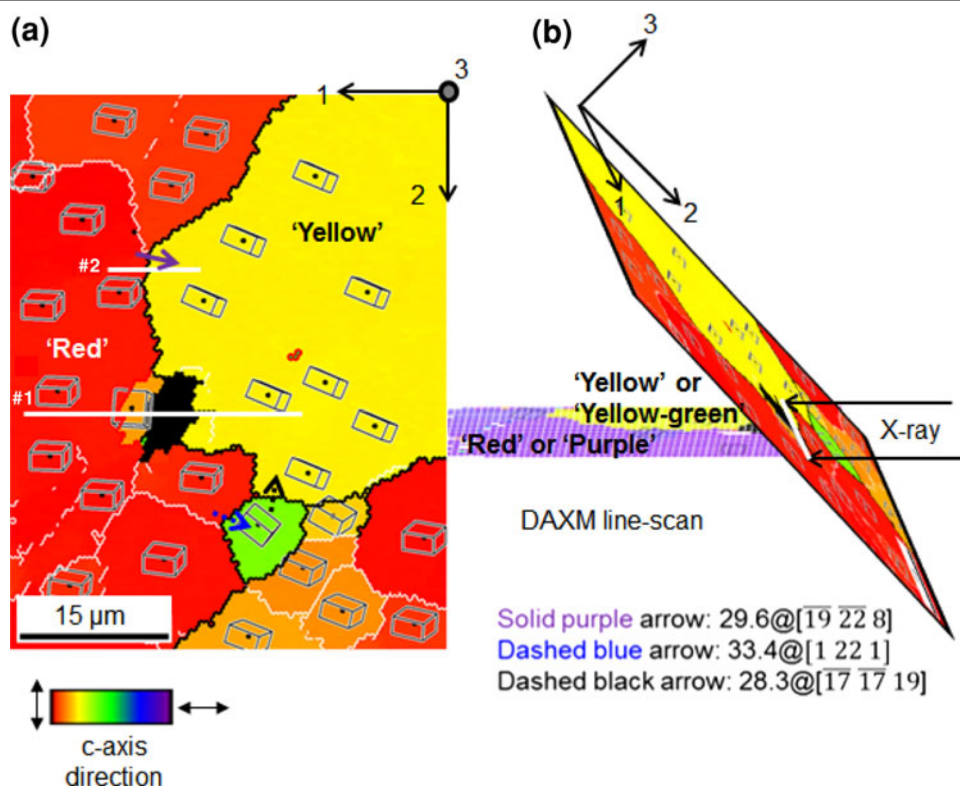

Fig. 4. (a) Two DAXM line scans (#1 and #2) across parent and recrystallized grains; (b) schematic showing the sampled diffraction volume beneath the surface and the corresponding Sn crystal orientation map (different color scale), and the coordinate system for the crystal orientations and the strain tensor; misorientation angle and rotation axes are noted for selected boundaries.

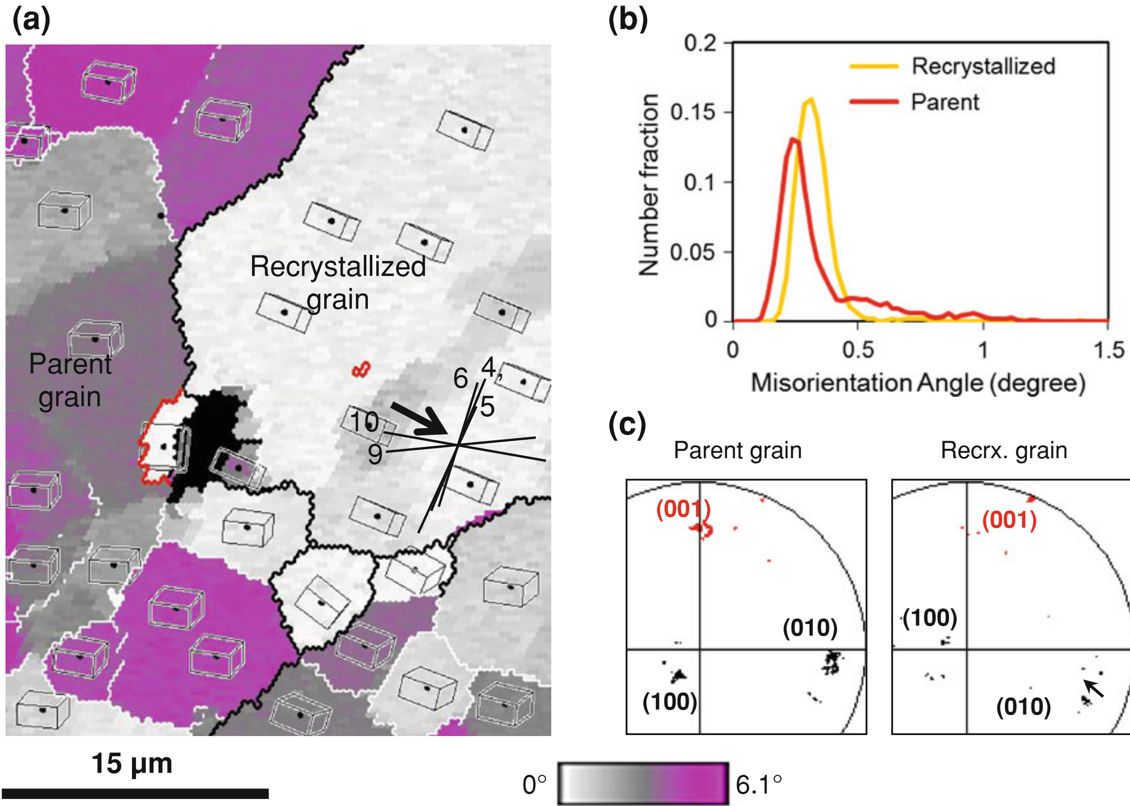

Fig. 5. (a) Grain reference orientation deviation map (6° spread from average orientation) of the same area as in Fig. 4a; slip traces of slip systems (SS) with highest m are shown; black arrow marks a subgrain boundary; low-angle, high-angle, and twin boundaries are displayed by white, black, and red lines, respectively; (b) local average misorientation (LAM) histogram and (c) overlaid 001 and 100 pole figures of the parent orientation and the recrystallized yellow grain in Fig. 4. (Color figure online).

Table I. Slip systems (SS) with highest Schmid factors (m) based upon the global stress, and corresponding rotation axes (RA) for edge (bold) or screw (normal font) dislocations

SS	#10	#4	#9	#6	#5	#5
n & b	$(\bar{1}21)[101]$	$(110)[\bar{1}11]$	$(10\bar{1})[101]$	$(010)[101]$	$(110)[1\bar{1}0]$	$(1\bar{1}0)[110]$
m	0.656	0.520	0.466	0.462	0.421	0.421
RA	$\sim[\mathbf{\bar{1}\bar{2}}4]$	$\sim[\mathbf{\bar{1}1\bar{7}}]$	$\sim[\mathbf{010}]$	$\sim[\bar{1}0\mathbf{3}]$	$\sim[\mathbf{001}]$	$\sim[\mathbf{00\bar{1}}]$
	$[\bar{1}23]$	$[110]$	$[10\bar{3}]$	$[010]$	$[110]$	$[1\bar{1}0]$

grain, the (001) and (010) peaks are split and/or broader. In contrast, the recrystallized grain shows barely any variation from the average orientation (as the map shows nearly homogeneous light grey). Nevertheless, near the interface with the Cu_6Sn_5 particle, larger misorientation regions (~3°, indicated by dark grey) are present.

Interestingly, the shift of the LAM distribution peak to larger angle in the recrystallized grain than the parent grain may be caused by the development of the light-grey band-like subgrain structure (Fig. 5a). This band-like structure with less than 2° misorientation from the average has gradual orientation gradients in color, particularly on the lower-right side of the band, and the boundary is sharper along the upper-left side of the band. Although this recrystallized grain was developed during thermal cycling, localized strain fluctuations led to subsequent heterogeneous deformation along the grey band within the grain, suggesting that this feature may be an active shear band within a newly recrystallized grain.

The difference in the orientation gradient on the two sides of the band suggests that a dislocation pile-up along the sharper upper-left subgrain boundary is likely. In order to correlate the local orientation gradient with slip activity, Schmid factors (m) of all 32 possible slip systems (SS) in Sn (grouped into ten families)[8] were calculated using an estimate of the global stress state. Assuming that simple shear due to the CTE mismatch is dominant during thermal cycling, the sense of shear parallel

to the solder/package interfaces is represented by a vector pointing from the solder ball to the geometric center of the package. The slip plane (n), slip direction (b), and corresponding lattice rotation axis (RA for both edge and screw dislocations) of the slip systems with the highest Schmid factors (larger than 0.42) are listed in Table I.

One slip system in SS family #10 has the highest Schmid factor, followed by #4, 9, 6, and 5. Slip traces of these slip systems are drawn on Fig. 5a, and the traces of SS #4, 5, and 6 are aligned close to the grey shear band. The boundary misorientation angle and rotation axis estimated from the EBSD data along the black arrow in Fig. 5a indicate 1.7° about the [$\bar{1}$16] axis (close to [001]). Rotation about the [001] axis is also evident in the recrystallized grain pole figure in Fig. 5c, where all the peaks are sharp except the (010) peak, which is elongated (rotated) about the (001) pole (black arrow). It has been reported in prior work that SS #10, 9, and 6 may be less facile,[27] so even though they have higher Schmid factor than SS #5, they may be less active. The slip band analysis is consistent with slip on (010), (110), and $\left(1\bar{1}0\right)$ planes, which excludes SS #9 and 10. In order to form a subgrain tilt boundary with edge dislocations by simple lattice rotation about [001] axis, $<$010], $<$111] or $<$110] dislocations should be mobile on {100} or {110} planes. However, for screw dislocations, Burgers vector $<$100] or $<$110] on {001} planes could lead to rotation about c-axis, but none of them have a high Schmid factor in this case. To satisfy all three criteria (m, RA, slip trace), edge dislocations in SS #4 and 5 are most likely to have been active. Nevertheless, Schmid factors calculated using the global stress state may not be representative of the local stress state, and thus the relative activity of different slip systems may vary from the condition estimated from the global Schmid factors.

The rotation of the Sn crystal lattice associated with slip activity and dislocation movement can also be analyzed using misorientation relationships between the parent orientation and the recrystallized grain, with consideration of the misorientations between the parent and neighboring recrystallized grains. Rather than a *single direct* rotation about a high-index axis indicated by the solid purple arrow in Fig. 4a, the recrystallized yellow orientation can be developed by a two-step lattice rotation sequence around low-index crystal directions: (1) dotted blue arrow: 33.4° @ [1 22 1] (close to [0 1 0]) to reach the green orientation, followed by (2) dotted black arrow: 28.3° @ [$\overline{17}$ $\overline{17}$ 19] (close to [$\bar{1}\bar{1}$1]) to reach the yellow orientation. (A similar relationship with a neighboring grain also exists beneath the sample surface, as discussed later.)

DAXM-BASED ANALYSIS

To capture the details of the Sn crystal orientation beneath the surface, DAXM was used for nondestructive assessment. Two DAXM line scans were

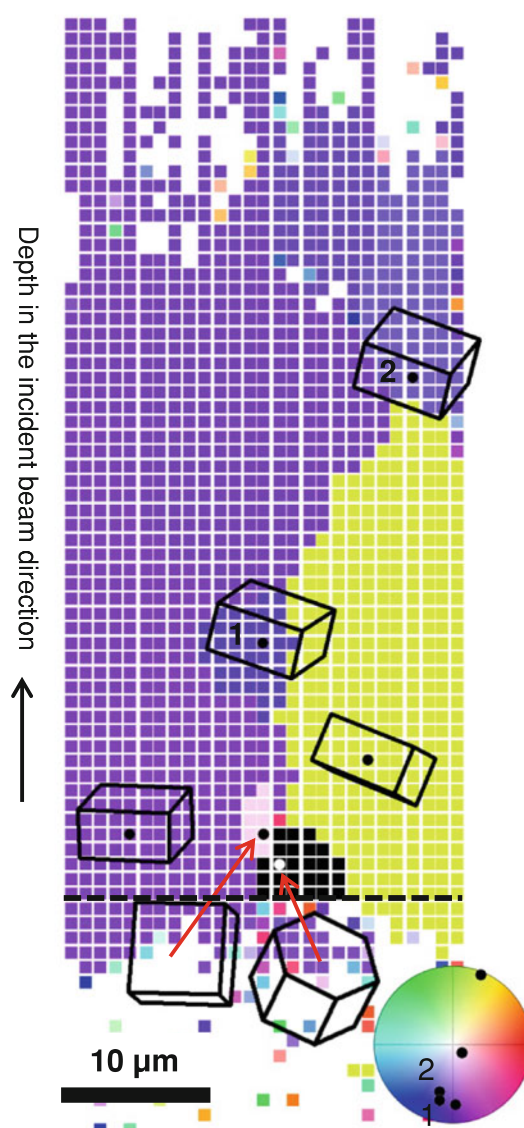

Fig. 6. DAXM subsurface orientation map and the reference color code (corresponding to 001 inverse pole figure) of line scan 1; crystal orientation of selected voxels of Sn and Cu_6Sn_5 phases are shown by prisms (and also labeled on the ipf colored sphere), and the corresponding Laue patterns are shown in Fig. 7. (Color figure online).

carried out, as shown in Fig. 4a. The longer, 27-μm line went across the center of the Cu_6Sn_5 particle, covering the parent red and small orange twin grains, IMC, and the recrystallized yellow orientation. The shorter, 17-μm line was 15 μm away from the first line, examining only the boundary between parent and recrystallized grains. In Fig. 4b, the sampled space beneath the surface and the corresponding orientation map are shown. The coordinate system used for DAXM and the internal strain calculation is the same as that used for the EBSD-based analysis. The automatic indexation and strain calculation from Laue measurements yield precise values of only the off-diagonal deviatoric strain tensor components[21] in Eq. 1. Hydrostatic strain components in the full strain tensor are not determined

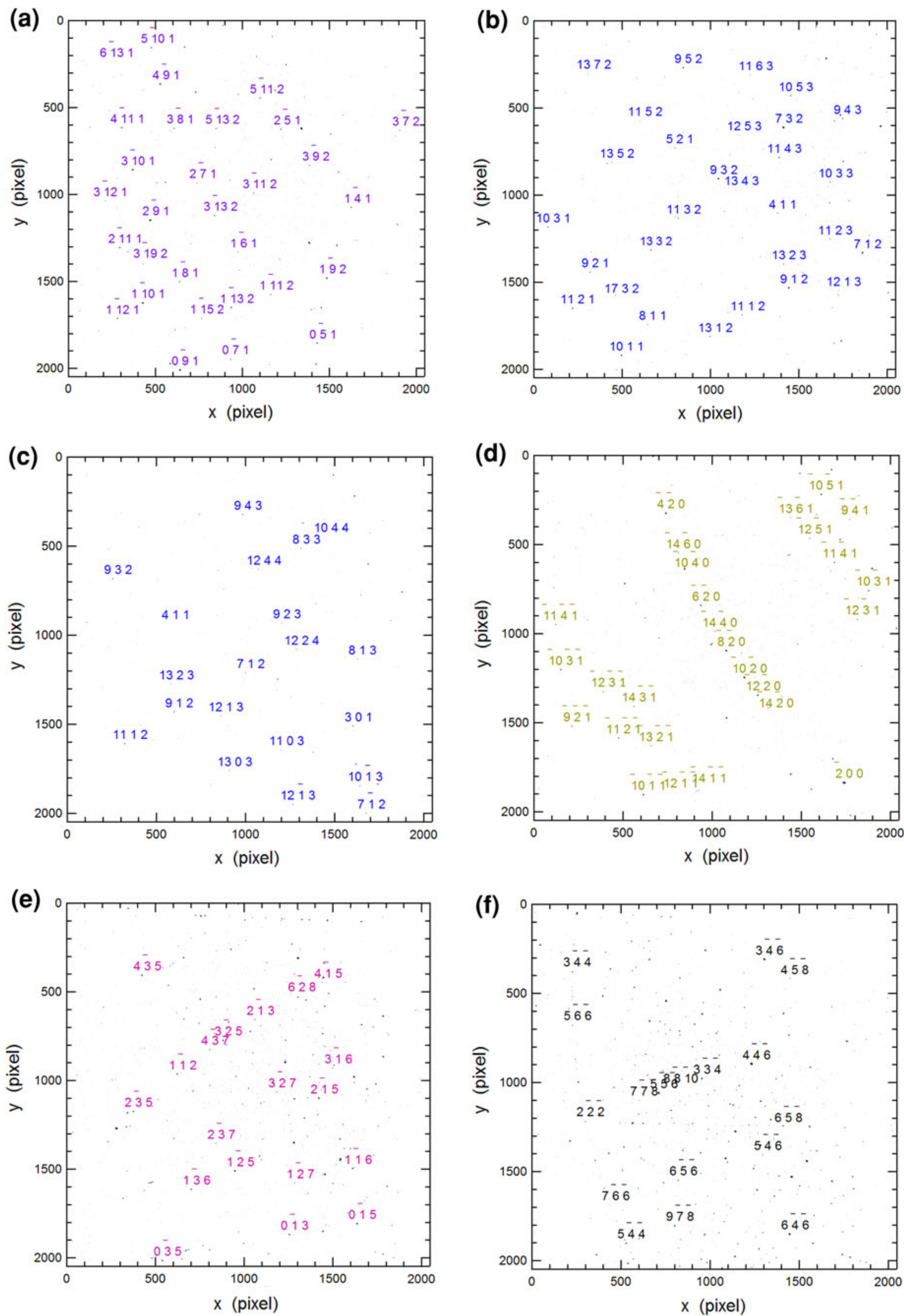

Fig. 7. Laue patterns from Sn and Cu_6Sn_5; the colors of indices correspond to different crystal orientations labeled in Fig. 6: (a) parent purple orientation; (b) ''blue 1'' grain; (c) ''blue 2'' grain; (d) recrystallized yellow orientation; (e) twin grain; (f) Cu_6Sn_5. (Color figure online).

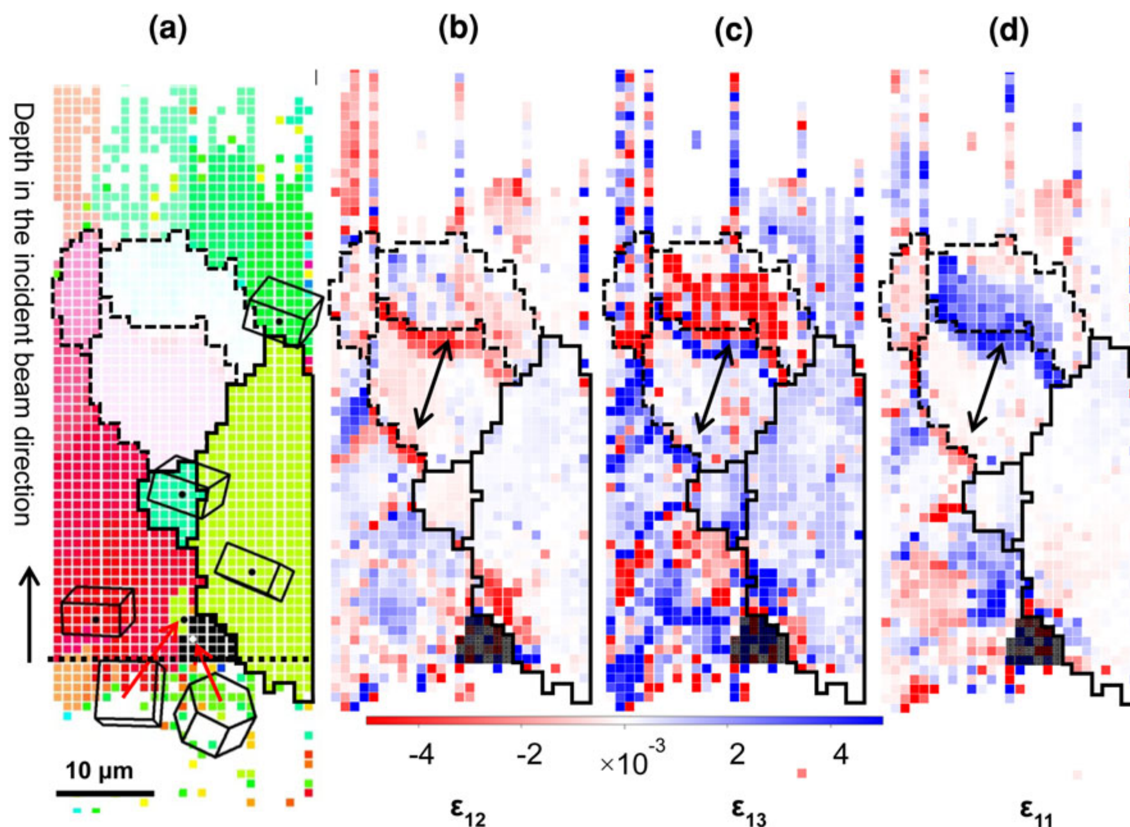

Fig. 8. (a) Sn and Cu_6Sn_5 unit cells, overlaid on an orientation map showing 3° misorientation spread (with white as reference orientation); grain boundaries between parent and recrystallized grain are solid lines, and subgrain boundaries are dashed lines; polished sample surface is approximately along the fine dashed line. Elements of the deviatoric strain tensor of Sn phase are plotted in (b–d) using the coordinate system in Fig. 4.

by this method, although the relative values are related via the parameter Δ, which can be quantified by measuring the energy of at least one reflection in Laue patterns.[21]

$$\varepsilon = \begin{pmatrix} \varepsilon'_{11} - \frac{\Delta}{3} & \varepsilon_{12} & \varepsilon_{13} \\ \varepsilon_{21} & \varepsilon'_{22} - \frac{\Delta}{3} & \varepsilon_{23} \\ \varepsilon_{31} & \varepsilon_{32} & \varepsilon'_{33} - \frac{\Delta}{3} \end{pmatrix} + \begin{pmatrix} \frac{\Delta}{3} & 0 & 0 \\ 0 & \frac{\Delta}{3} & 0 \\ 0 & 0 & \frac{\Delta}{3} \end{pmatrix} \quad \text{where } \Delta = \varepsilon'_{11} + \varepsilon'_{22} + \varepsilon'_{33} \tag{1}$$

Using this coordinate system, the shear strains due to package-scale CTE mismatches between solder/chip/substrate are represented by a combination of ε_{12} and ε_{13}. During thermal cycling, tensile/compressive strains due to the difference in thermal expansion arising from the joint crystal orientation normal to the package interface are represented by ε_{11}. The Sn crystal orientation and its effect on the strain gradient are discussed below.

As shown in Fig. 6, a DAXM orientation map shows various grains on and beneath the sample surface, and selected diffraction patterns are shown in Fig. 7. Crystal orientations are represented by the sample normal inverse pole figure key. At the center of the colored sphere, white is used as the reference color. Thus, for each voxel, its color shows the orientation of the (001) pole on the color sphere. In order to examine small orientation gradients, "white" can be assigned to any orientation, and the radius of the new color sphere corresponds to the deviation from the reference orientation. Consequently, local orientation gradients can be illustrated by different colors, as shown in Fig. 8a. As this map shows the subsurface region, the physical (initially polished) surface is approximately at the black dotted line. The Cu_6Sn_5 particle was manually indexed at each of the black voxels. Three Sn grain orientations (purple, pink, and yellow–green) near the sample surface in Fig. 6 match the EBSD red, orange, and yellow results in Fig. 4a, respectively. Two additional Sn crystal orientations (blue 1 and 2 in Fig. 6) beneath the surface are also revealed. The misorientation relationships between the different Sn grains are listed in Fig. 9. No grain boundary misorientation is correlated with any known special boundary in Sn,[26] other than the twin misorientation between the pink and purple grains. Nevertheless, the rotation axis between grain blue 1 and the recrystallized yellow grain is $[2\,16\,\bar{1}]$, which is

	Purple	Yellow-green	Blue 1	Blue 2	Pink
Purple	**(272, 74, 166)**	30@ $[14\,17\,\bar{6}]$	16.4@$[1\,\overline{16}\,13]$	19.1@$[14\,6\,\bar{5}]$	**61.9@[30 0 1]**
Yellow-green		**(247, 92, 254)**	22.4@$[2\,16\,\bar{1}]$	30.2@$[1\,28\,\overline{10}]$	86.9@$[21\,4\,\bar{7}]$
Blue 1			**(256, 71, 73)**	9.2@$[\bar{7}\,19\,20]$	64.8@$[18\,\bar{3}\,8]$
Blue 2				**(255, 63, 78)**	57.2@$[27\,\bar{7}\,12]$
Pink					**(316, 18, 131)**

Fig. 9. Euler angles of different Sn crystal orientations (on diagonal) and their misorientation relationships (misorientation angle in degrees and rotation axis). (Color figure online).

close to the [010] (a-axis). In contrast, in order to develop the yellow–green orientation *directly* from purple orientation, the Sn crystal lattice needs to rotate 30° about $[14\,17\,\bar{6}]$ (close to $[2\,3\,\bar{1}]$) axis. As with the observations discussed for the intermediate green grain in Fig. 4a, it is possible that continuous recrystallization may have occurred by two independent processes by the rotations (1) from parent purple orientation to "blue 1" orientation (lower angle about "$c + a$" $[0\bar{1}1]$ axis), and (2) from "blue 1" to "yellow" around the a-axis. However, from a similar analysis of slip system activities as discussed above, no slip system with high global Schmid factor is likely to cause these rotations. It is thus inferred that lattice rotation by larger angles (16° and 22°) may not be accomplished by the activation of a single dominant slip system.

Laue patterns from selected diffraction volume elements (voxels) identified in Fig. 6 are manually indexed in Fig. 7. Laue patterns from Sn are shown in Fig. 7a–e and for Cu_6Sn_5 phase in Fig. 7f using the same grain color code to label orientations and indices in Fig. 6. These diffraction spots are sharp with no apparent streaks. Furthermore, there is no dramatic difference in the shape of Sn diffraction peaks between the parent grain (Fig. 7a) and the recrystallized grain in Fig. 7d, suggesting that, within each 1 μm^3 voxel, the local geometrically necessary dislocation (GND) content is low regardless of whether the grain is recrystallized or not. At this scale, a streaked peak would be caused by bent crystal planes due to the presence of local GNDs rather than low-angle boundaries. The lack of streaked peaks implies that, during thermal cycling, GNDs generated by heterogeneous strain are efficiently absorbed at existing subgrain boundaries, leaving few unpaired dislocations in the lattice. Moreover, given that ambient temperature is $\sim 0.6 T_m$, dislocation climb could have been active prior to measurements to reduce local GND content.

The existence of many low-angle boundaries contributing to streaked diffraction peaks has been reported in prior work[3,8] in which the whole volume of the solder joint (larger than 0.01 mm^3) was sampled using a monochromatic transmission x-ray beam. Streaked Sn diffraction peaks in solder balls were observed right after solidification, and the strain arising from the CTE mismatch during cooling did not change the magnitude of the streak. The existence of low-angle boundaries and orientation gradients even before thermal cycling began contributed to streaked diffraction peaks, though these streaks increased in magnitude with thermal cycling.

Components of the elastic strain tensor were extracted from Laue microdiffraction patterns,[21] and the values are plotted in Fig. 8 for each voxel using the color scale shown. The calculation of elastic strain was performed based on the Sn crystal structure, so the region where Cu_6Sn_5 is present is shaded dark grey. The ε_{11} normal strain perpendicular to the package interface is plotted in Fig. 8d. The values have the same range of magnitude as the scale for the shear components, but the actual numerical values are not known (due to the unknown Δ). During thermal cycling, the shear stress imposed on solder balls is related to the relative position of the ball with respect to the neutral point (geometric center of the package); For instance, the sense of shear in ball 5 is on the plane defined by directions 2 and 3 in Fig. 2a. Therefore, a combination of ε_{12} and ε_{13} in Fig. 8b, c represents the probable maximum shear strain on the interface plane between the solder and package. With the dominant Sn crystal orientation known, it is expected that this solder ball also experienced tensile strain normal to the package interface during high temperature, and compressive strain at low temperature, so at room temperature it should be more compressive than tensile, which is consistent with the observed relative difference in the ε_{11} strain.

As shown in Fig. 8b–d, the heterogeneous distribution of residual strain varies among different

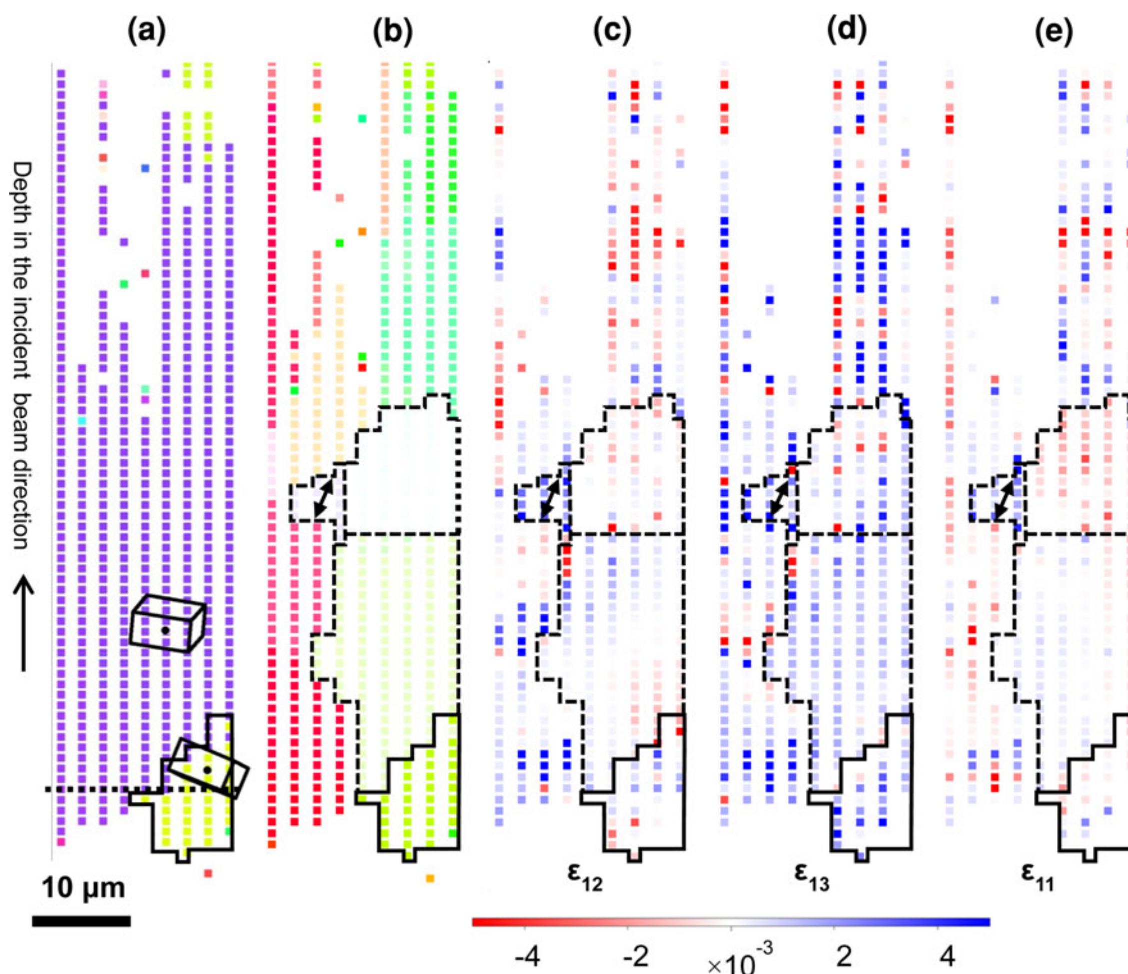

Fig. 10. (a) DAXM orientation map of line scan #2 reveals parent purple orientation and the recrystallized yellow grain; 3° orientation spread is shown in (b); elements of deviatoric strain tensor of Sn phase are plotted in (c–e) using the coordinate system in Fig. 4. Subgrain boundaries are highlighted by black dashed lines, and solid lines for high-angle boundaries. (Color figure online).

crystal orientations, as well as inside a single grain or subgrain. High-angle grain boundaries are indicated by bold lines, and dashed lines identify low-angle or subgrain boundaries. In contrast to the dominant red orientation (also red in Fig. 8a), recrystallized grains (light and yellow–green) are nearly free of residual shear and normal strains (ε_{12} and ε_{11}), but a residual ε_{13} shear strain of around 0.1% is distributed homogeneously in the same recrystallized grains. Due to the relative location of ball 5 in the array, the total shear strain can be approximated by the sum of ε_{12} and ε_{13}. By combining Fig. 8b and c, the residual shear strains in the recrystallized grains still have near-zero values.

Due to the presence of the large Cu_6Sn_5 IMC particle, both shear and normal residual strains (Fig. 8b–d) are present near the particle in Fig. 8a) in both the recrystallized and parent grains. Farther from the large IMC, the strains are smaller in magnitude. Higher residual strain values can also be found near some low-angle/subgrain boundaries (black arrows and dashed lines) in the parent Sn orientation, where subgrain boundaries (as clearly shown in the 3° misorientation spread map in Fig. 8a) contribute to the local strain concentration. Consequently, the difference in residual strain distribution beneath the sample surface reflects internal strains arising from microstructure evolution during thermal cycling, combined with room-temperature aging/recovery effects when the sample was stored isothermally before being examined using DAXM.

The other line scan (#2) reveals the crystal orientation and strain distribution beneath the sample surface across another portion of the same grain boundary between the parent and the recrystallized grain, as shown in Fig. 10. Two crystal orientations are present, as displayed by prisms in Fig. 10a. In contrast to Fig. 5, no additional Sn orientations are found other than those revealed by EBSD, though there are a few subgrain boundaries present (marked by dashed lines). The similar orientation gradients and low-angle boundaries contributed to the heterogeneous distribution of elastic strains.

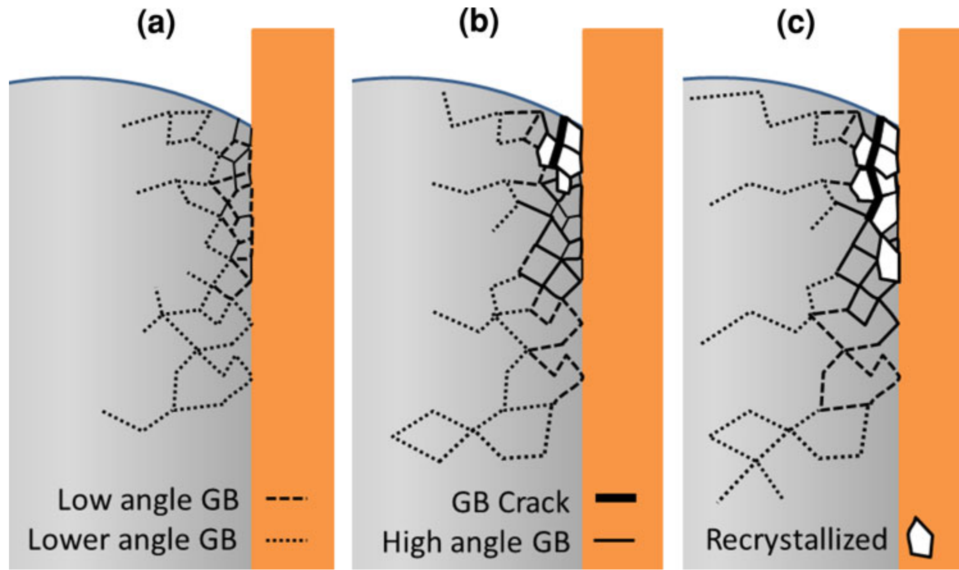

Fig. 11. (a) Subgrain formation, with higher misorientation and smaller size corresponding to more solid line in the higher-stress region; (b) some subgrain boundaries become mobile with dissolution of some precipitates, and sweep out dislocations in subgrain boundaries, making more perfect crystals. Some of the more mobile boundaries have higher energy and less cohesive force, and can slide and/or crack; (c) further dissolution/coarsening of precipitates releases other boundaries to move, propagating the same process as in (b, c).

Lower ε_{12} and ε_{11} values are found for the recrystallized grain, as well as its adjacent subgrain (marked by dashed black lines in Fig. 10). In the same region, about 0.1% shear strain in the 1–3 direction (ε_{13}) is distributed homogeneously, similar to in Fig. 8c. However, in the rest of the parent grain, strains are distributed quite heterogeneously, and vary in different subgrain orientations. As indicated by the arrows (Fig. 10b–e), this light-purple subgrain exhibits higher shear and normal strain than its neighbors. Compared with line scan #1, the lack of large IMC precipitates in Fig. 10 may account for the smaller strains at the recrystallized boundaries.

RECRYSTALLIZATION MECHANISMS

In prior work, a continuous recrystallization mechanism was proposed to account for the systematic and gradual changes in grain orientations.[8] If the subgrain boundaries that developed into high-angle boundaries retained their geometrical positions, then it is possible that internal strains and orientation gradients would be retained. On the other hand, if coarsening of the particles that pinned the evolving subgrain boundaries occurred, then the continuously recrystallized subgrain boundaries could achieve increased mobility, and thus move into neighboring grains and subgrains. This grain boundary migration would leave behind a more perfect crystal, such as the clearly recrystallized orientations that show a lack of internal strains and orientation gradients (white or light grey in GROD maps). This process is schematically illustrated in Fig. 11. This form of boundary migration may be considered similar to primary recrystallization (because moving boundaries sweep out defects in subgrains that show internal strains), but continuous recrystallization accounts for the process of generating a stable grain that would grow into other subgrains. This form of primary recrystallization follows the paradigm of oriented nucleation, where nuclei arise by generation of continuously recrystallized subgrains that form closest to the interface between the solder joint and the package where the stresses are highest. In Ref. 8, recrystallization by continuous recrystallization was proposed as the dominant mechanism. In this analysis, it appears that continuous recrystallization sets up the possibility for an oriented nucleation primary recrystallization process in the areas that experienced the greatest amount of strain, and thence cracked along selected grain boundaries. This difference in the interpretation of the recrystallization process from that in Ref. 8 was enabled by GROD maps and the internal strain information obtained using DAXM. The primary recrystallization process is less developed in the lower parts of the microstructure in Fig. 3e. Thus, it appears that just about any form of recrystallization can occur locally, and the details depend on the history of locally activated slip systems.

CONCLUSIONS

Observations using EBSD and DAXM 3D x-ray microscopy indicated that continuous recrystallization processes lead to formation of orientations that are able to grow into adjacent regions similar to an oriented nucleation primary recrystallization mechanism in the regions ahead of crack propagation. Development of a large number of low-angle boundaries in the parent orientation precedes the formation of recrystallized grains. Crack propagation

proceeded mainly along recrystallized grain boundaries. In newly recrystallized grains, further deformation may trigger subgrain formation by slip and lattice rotation, revealed as a distinct local orientation gradient. DAXM Laue patterns show no streaks in Sn peaks, indicating low GND content in the 1 μm^3 voxels. The reduced local GND may be a combined effect of (1) absorption by preexisting subgrain boundaries, and (2) a recovery process during storage at room temperature.

ACKNOWLEDGEMENTS

This work is supported by NSF-GOALI Contract 1006656 and Cisco Systems Inc., San Jose, CA. Use of the Advanced Photon Source was supported by the US Department of Energy, Office of Science, Office of Basic Energy Sciences, under Contract No. DE-AC02-06CH11357.

REFERENCES

1. J.W. Elmer, E.D. Specht, and M. Kumar, *J. Electron. Mater.* 39, 273 (2010).
2. G.J. Jackson, H. Lu, R. Durairaj, N. Hoo, C. Bailey, N.N. Ekere, and J. Wright, *J. Electron. Mater.* 33, 1524 (2004).
3. B. Zhou, T.R. Bieler, G. Wu, S. Zaefferer, T.-K. Lee, and K.-C. Liu, *J. Electron. Mater.* 41, 262 (2012).
4. A. Pietrikova, J. Bednarcik, and J. Durisin, *J. Alloy. Compd.* 509, 1550 (2011).
5. K.-J. Wang, Y.-C. Lin, J.-G. Duh, C.-Y. Cheng, and J.-J. Lee, *J. Mater. Res.* 25, 972 (2010).
6. J.O. Suh, K.N. Tu, and N. Tamura, *JOM* 58, 63 (2006).
7. D. Mu, J. Read, Y. Yang, and K. Nogita, *J. Mater. Res.* 26, 2660 (2011).
8. T.R. Bieler, B. Zhou, L. Blair, A. Zamiri, P. Darbandi, F. Pourboghrat, T.-K. Lee, and K.-C. Liu, *J. Electron. Mater.* 41, 283 (2012).
9. W.J. Choi, T.Y. Lee, K.N. Tu, N. Tamura, R.S. Celestre, A.A. MacDowell, Y.Y. Bong, and L. Nguyen, *Acta Mater.* 51, 6253 (2003).
10. M. Sobiech, M. Wohlschlögel, U. Welzel, E.J. Mittemeijer, W. Hügel, A. Seekamp, W. Liu, and G.E. Ice, *Appl. Phys. Lett.* 94, 221901 (2009).
11. K.N. Tu, C. Chen, and A.T. Wu, *J. Mater. Sci.-Mater. Electron.* 18, 269 (2007).
12. T.-K. Lee, W. Xie, B. Zhou, T.R. Bieler, and K.-C. Liu, *J. Electron. Mater.* 40, 1967 (2011).
13. G.E. Ice, J.D. Budai, and J.W.L. Pang, *Science* 334, 1234 (2011).
14. G.E. Ice and R.I. Barabash, *Dislocations in Solids*, ed. F.R.N. Nabarro and J.P. Hirth (Amsterdam: Elsevier, 2007), p. 500.
15. B.C. Larson, W. Yang, G.E. Ice, J.D. Budai, and J.Z. Tischler, *Nature* 415, 887 (2002).
16. W. Liu, G.E. Ice, B.C. Larson, W. Yang, and J.Z. Tischler, *Ultramicroscopy* 103, 199 (2005).
17. W. Liu, G.E. Ice, B.C. Larson, W. Yang, J.Z. Tischler, and J.D. Budai, *Metall. Mater. Trans. A* 35A, 1963 (2004).
18. L. Yin, L. Wentlent, L. Yang, B. Arfaei, A. Oasaimeh, and P. Borgesen, *J. Electron. Mater.* 41, 241 (2012).
19. D.W. Henderson, J.J. Woods, T.A. Gosselin, J. Bartelo, D.E. King, T.M. Korhonen, M.A. Korhonen, L.P. Lehman, E.J. Cotts, S.K. Kang, P. Lauro, D.-Y. Shih, C. Goldsmith, and K.J. Puttlitz, *J. Mater. Res.* 19, 1608 (2004).
20. H. Chen, J. Han, and M. Li, *J. Electron. Mater.* 40, 2470 (2011).
21. G.E. Ice, B.C. Larson, J.Z. Tischler, W. Liu, and W. Yang, *Mater. Sci. Eng. A-Struct.* 399, 43 (2005).
22. R.D. Doherty, D.A. Hughes, F.J. Humphreys, J.J. Jonas, D.J. Jensen, M.E. Kassner, W.E. King, T.R. McNelley, H.J. McQueen, and A.D. Rollett, *Mater. Sci. Eng. A-Struct.* 238, 219 (1997).
23. J. Li, H. Xu, T.T. Mattila, J.K. Kivilahti, T. Laurila, and M. Paulasto-Kröckel, *Comput. Mater. Sci.* 50, 690 (2010).
24. http://www.aps.anl.gov/Sectors/33_34/microdiff/.
25. A.-K. Larsson, L. Stenberg, and S. Lidin, *Acta Crystall. B-Struct.* B50, 636 (1994).
26. A.U. Telang and T.R. Bieler, *JOM* 57, 44 (2005).
27. B. Zhou, T.R. Bieler, T.-K. Lee, and K.-C. Liu, *J. Electron. Mater.* 39, 2669 (2010).
28. T.-K. Lee, B. Zhou, L. Blair, K.-C. Liu, and T.R. Bieler, *J. Electron. Mater.* 39, 2588 (2010).
29. M.A. Matin, E.W.C. Coenen, W.P. Vellinga, and M.G.D. Geers, *Scripta Mater.* 53, 927 (2005).